

This is an Open Access document downloaded from ORCA, Cardiff University's institutional repository:<https://orca.cardiff.ac.uk/id/eprint/127492/>

This is the author's version of a work that was submitted to / accepted for publication.

Citation for final published version:

Zeng, Zhenzhong, Ziegler, Alan D., Searchinger, Timothy, Yang, Long, Chen, Anping, Ju, Kunlu, Piao, Shilong, Li, Laurent Z. X., Ciais, Philippe, Chen, Deliang, Liu, Junguo, Azorin-Molina, Cesar, Chappell, Adrian, Medvigy, David and Wood, Eric F. 2019. A reversal in global terrestrial stilling and its implications for wind energy production. *Nature Climate Change* 9 (12), pp. 979-985. 10.1038/s41558-019-0622-6

Publishers page: <http://dx.doi.org/10.1038/s41558-019-0622-6>

Please note:

Changes made as a result of publishing processes such as copy-editing, formatting and page numbers may not be reflected in this version. For the definitive version of this publication, please refer to the published source. You are advised to consult the publisher's version if you wish to cite this paper.

This version is being made available in accordance with publisher policies. See <http://orca.cf.ac.uk/policies.html> for usage policies. Copyright and moral rights for publications made available in ORCA are retained by the copyright holders.



33 **Wind power is a rapidly growing alternative energy source to achieve the goal of the Paris**
34 **Agreement under the United Nations Framework Convention on Climate Change, to keep**
35 **warming well below 2 °C by the end of the 21st century. Widely reported reductions in global**
36 **average surface wind speed since the 1980s, known as terrestrial stilling, however, have gone**
37 **unexplained and have been considered a threat to global wind power production. Our new**
38 **analysis of wind data from *in-situ* stations worldwide now shows that terrestrial stilling**
39 **reversed around 2010 and global wind speeds over land have recovered most of the losses**
40 **since the 1980s. Concomitant increased surface roughness from forest growth and**
41 **urbanization cannot explain prior stilling. Instead we show decadal-scale variations of near-**
42 **surface wind are very / quite likely caused by the natural, internal decadal ocean/atmosphere**
43 **oscillations of the Earth's climate system. The wind strengthening has increased the amount**
44 **of wind energy entering turbines by $17 \pm 2\%$ for 2010-2017, likely increasing U.S. wind power**
45 **capacity by 2.5%. The increase in global terrestrial wind bodes well for the immediate future**
46 **of wind energy production in these regions as an alternative to fossil fuel consumption.**
47 **Projecting future wind speeds using ocean/atmosphere oscillations show wind turbines could**
48 **be optimized for expected wind speeds, including small and large speeds, during the**
49 **productive life spans of the turbines.**

50
51 Reports of a 8% global decline in land surface wind speed (~1980 to 2010) have raised concerns
52 about output from future wind power¹⁻⁵. Wind power varies with the cube of wind speed (u)⁶. The
53 decline in wind speed is evident in the northern mid-latitude countries where the majority of wind
54 turbines are installed including China, the U.S. and Europe¹. If the observed 1980-2010 decline in
55 wind speed continued until the end of the century, global u would reduce by 21%, halving the
56 amount of power available in the wind. Understanding the drivers of this long-term decline in wind

57 speed is critical not merely to maximize wind energy production⁹⁻¹¹ but also to address other
58 globally significant environmental problems related to stilling, including reduced aerosol dispersal,
59 reduced evapotranspiration rates, and adverse effects on animal behavior and ecosystem
60 functioning^{1,3,4,12}.

61

62 The potential causes for the global terrestrial stilling are complex and remain contested (e.g.,
63 Vautard et al., 2010; McVicar et al., 2012; Torralba et al., 2017; Wu et al., 2018). Terrestrial
64 surface winds are driven by atmosphere circulations and momentum extracted by rough land
65 surface. Many regional-scale studies using reanalysis datasets have found correlations of u to some
66 climate indices (e.g., Chen and Pryor, 2013; Nchaba et al., 2017; Naizghi and Quarda, 2017;
67 Azorin-Molina et al., 2018). Those studies hypothesize that the terrestrial stilling is caused by
68 decreased driving force due to the change in large scale circulations (Torralba et al., 2017). The
69 hypothesis is supported by the consistency between the wind speed changes at the surface and at
70 higher levels in the reanalysis datasets (Refs???) Consistent wind speed change cannot be
71 explained by change in land surface (Chen and Pryor, 2013; Torralba et al., 2017). However, there
72 are no feedbacks between land surface change, aerodynamic roughness and wind speed i.e., wind
73 speed reanalysis data does not represent land surface dynamics. There are large uncertainties in the
74 reanalysis datasets (e.g., Vautard et al., 2010; Chen and Pryor, 2013; Torralba et al., 2017) and,
75 more importantly, the global terrestrial stilling is either not reproduced or has been largely
76 underestimated in global reanalysis products^{2,8} (Supplementary Fig. 1) or climate model
77 simulations for IPCC AR5 (Supplementary Fig. 2). The discrepancies between the decreasing
78 trends derived from *in situ* stations and from reanalysis or climate model simulations lead to an
79 alternative hypothesis. Global terrestrial stilling is caused by increased drag from increased land

80 surface roughness from global ‘greening’ of the Earth and/or urbanization^{2,7}, both of which would
81 suggest further future declines.

82

83 Recent studies have described wind speed reversal at local scales^{16,17} (Tobin et al. 2014, Kim and
84 Paik 2015) or in annual climate reports at global scale¹⁸ (Tobin et al. 2014). However, there is no
85 clear global trend of wind speed change (e.g. refs 5, 8). A wind reversal could elucidate the causes
86 of global terrestrial stilling and potentially improve our future wind energy projections. We
87 investigated changes in recent global wind speeds and revealed three key findings: (1) global
88 stilling reversed-2009-2011 and recovered most of the wind speed over land lost between 1980 and
89 2010; (2) a strong correlation (r value and p-value?) between global and regional wind speeds over
90 land and decadal changes in global ocean/atmosphere oscillations; (3) recovered terrestrial wind
91 speed explains much of the increase in U.S. wind power capacity over the last decade. These recent
92 phases of the ocean/atmosphere oscillations are likely to continue for at least another decade
93 (references 22,24,25,27,35). Consequently, these changes are promising for future wind power
94 generation in that time period. However, our findings also suggest that wind power output is very
95 (or how much) likely to fluctuate over decadal timescales, which will require appropriate planning
96 of wind turbines.

97

98 Our analysis of global land surface wind speed change integrates direct *in situ* observations of *u*
99 from terrestrial weather stations from 1978 to 2017 together with statistical models for detection
100 of trends. The XXXX stations used were selected carefully from a total of 28,149 stations in the
101 Global Summary of Day (GSOD) database following strict quality control procedures
102 (Supplementary Fig. 3; see *Methods* for details). They are mainly distributed in the northern mid-

103 latitudes countries, including nine of the top 10 cumulative wind power capacity countries: China,
104 USA, Germany, India, Spain, UK, France, Canada, and Italy¹³. As one of our goals is to test for a
105 continuation of the terrestrial stilling after 2010 (refs 1-3), we use a piecewise linear regression
106 model to examine the potential trend changes^{14,15}.

107 108 **Extent reversal in global terrestrial stilling**

109 Our analysis shows that global mean annual u decreased significantly at a rate of -0.08 m s^{-1} (or -
110 2.3%) per decade during the first three decades beginning in 1978 (P-value < 0.001; Fig. 1a,
111 Supplementary Table 1). The decreasing trend echoes results of prior studies²⁻⁴ and confirms global
112 terrestrial stilling as an established phenomenon during the period of 1978-2010. However, u has
113 significantly increased in the current decade. This turning point is statistically significant at $P <$
114 0.001 with a goodness of fit of an $R^2 = 90\%$ (Fig. 1a). The recent increasing rate of $+0.24 \text{ m s}^{-1}$
115 decade^{-1} ($P < 0.001$) is three times that of the decreasing rate, before the turning point in 2010.
116 Below (where?) Next? we provide robust and comprehensive evidence that the reversal is global
117 and changing at the decadal scale and is not associated with regional events or occurring at random.

118
119 To exclude the possibility that the turning point is caused by large wind speed changes at only a
120 few sites, we repeat our analyses 300 times by randomly resampling 40% of the global stations
121 each time (grey lines in Fig. 1a; 40% of the stations are selected to ensure a sufficient sample size
122 ($n > 500$)). We find significant turning points in each randomly-selected sub-sample ($P < 0.001$;
123 $R^2 \geq 76\%$). Run-specific turning points occur between 2002 and 2011, with most (95%) of them
124 between 2009 and 2011 (Fig. 1b). In addition, mean annual u changes before and after a specific
125 turning point based on the 300 sub-sample estimates are $-0.08 \pm 0.01 \text{ m s}^{-1}$ per decade and $0.24 \pm$

126 0.03 m s⁻¹ per decade, respectively (Fig. 1c), identical to those values based on all the global
127 samples.

128
129 Spatial analyses further confirm that the recent reversal is a global-scale phenomenon
130 (Supplementary Fig. 4a-c). A majority (79%) of the stations where u decreased significantly during
131 1978-2010 (Supplementary Fig. 4b) have positive trends in u after 2010 (Supplementary Fig. 4c).
132 The stations are mainly distributed over three regions: North America (USA and Canada), Europe
133 (Germany, Spain, United Kingdom, France and Italy), and Asia (mainly China and India).
134 Significant turning points exist in all of the regions mean annual u time series ($P < 0.001$,
135 Supplementary Fig. 4d-f), but they vary in the specific year of occurrence. For example, a turning
136 point occurs earlier in Asia (2001, $R^2 = 80\%$, Supplementary Fig. 4f) and Europe (2003, $R^2 = 56\%$,
137 Supplementary Fig. 4e) than in North America (2012, $R^2 = 80\%$, Supplementary Fig. 4d).
138 Nevertheless, all regions show a significant increase in u after ~2010 (Supplementary Fig. 4d-f).

139
140 The existence of turning points is robust regardless of month (Supplementary Table 1 and
141 Supplementary Fig. 5) or wind variable chosen for analysis (Supplementary Fig. 6), and shows no
142 dependence on quality control procedures for weather station data (Supplementary Fig. 7).
143 Furthermore, we show that our findings are robust and repeatable (Supplementary Fig. 8) using a
144 different data set—the HadISD database. The HadISD database passes similar stringent station
145 selection criteria and quality control tests established by Met Office Hadley Centre¹⁹. In both
146 datasets??? we find that the tendency for an increasing number of stations becoming automated
147 during recent decades (Supplementary Figs 9 and 10) does not affect the result (Supplementary
148 Fig. 11). To test the effect of inhomogeneity, we remove all the stations with change point as

149 detected by the Pettit test (Pettitt, 1979), repeat the analyses and find the results have not changed
150 (Supplementary Fig. 12). All these lines of evidence supports our finding that the trends in u are
151 not caused by changes in measurement or other systematic errors in the measurement network.

153 **Causes of the reversal in global terrestrial stilling**

154 Next we explore causes of decadal changes in u over land. To explain the early global stilling,
155 researchers have offered a variety of theories, many of which are focused on the drag force of u
156 linked to terrestrial roughness including urbanization and vegetation changes². These theories have
157 been disputed²⁰ (also see Supplementary Figs 13 and 14). However, we find that global stilling
158 changed abruptly after 2010 which is inconsistent with typically slow change in terrestrial
159 roughness. The variation in u (including prior stilling and the recent reversal) is most likely caused
160 by driving forces associated with decadal variability of large-scale ocean/atmospheric circulations.
161 An extensive literature describes change in ocean/atmosphere oscillations, cause adjustments in
162 global circulation, generate stationary atmospheric waves, and lead to massive reorganizations of
163 u patterns²¹⁻²⁵ (Chen and Pryor, 2013; Kim and Paik, 2015; Nchaba et al., 2017; Naizghi and
164 Quarda, 2017; Azorin-Molina et al., 2018). The relationship between these oscillations and long-
165 term wind speeds over the entire globe has not been well established.

166
167 We investigate whether decadal ocean/atmosphere oscillations can explain these decadal changes
168 in u over land. Essentially, wind is physically caused by the uneven heating of the Earth surface
169 (temperature anomalies or heterogeneity), and the latter is widely described by climate indices
170 for oscillations (see *Methods*). To test such associations, we use 21 indicators of ocean/atmosphere
171 oscillations which are well-known and provide information about the decadal variations of

172 ocean/atmospheric circulations (see description in Supplementary Table 2). These indices are
173 characterized with the observed regional sea surface temperature and pressure anomalies
174 (*Methods*). Second, to avoid overfitting with multiple indices, we apply stepwise regression²⁶ to
175 identify the six largest explanatory power factors for the decadal variations of u over regions of
176 the globe, North America, Europe, and Asia, respectively (results in Supplementary Table 3).
177 Multiple regression of these six indices (Supplementary Table 3) reconstruct decadal variations of
178 u over the globe with an R^2 of $70 \pm 5\%$ ($79 \pm 2\%$ for North America, $48 \pm 9\%$ for Europe, and 51
179 $\pm 8\%$ for Asia; Supplementary Fig. 15).

180

181 To ensure that the correlations are not due to the trend in these data, we detrended all the time
182 series and repeated the stepwise regression analysis. The goodness of fit decreased because the
183 correlation related to the long-term stilling has been largely removed after detrending
184 (Supplementary Fig. 16). However, these detrended indices still significantly and substantially
185 explain the detrended variation of u , particularly for the recent rapid reversal (Supplementary Fig.
186 16). Furthermore, we train our models only using the detrended time series before the turning
187 points (2010 for the globe, 2012 for North America, 2003 for Europe, and 2001 for Asia), and find
188 that the models are capable to reproduce well the positive trends after the turning points for the
189 globe ($P < 0.001$; Fig. 2a), and all three regions ($P < 0.001$; Fig. 2b-d). The magnitude of the
190 increasing rate after the turning points is well modelled (Fig. 2). These results demonstrate that the
191 ocean/atmosphere oscillations are the key drivers for the recent, rapid reversal of the terrestrial
192 stilling.

193

194 The greatest explanatory power factor for each region is associated with the following indices:
195 Tropical Northern Atlantic Index (TNA) for North America ($R = -0.67$, $P < 0.001$); North Atlantic
196 Oscillation (NAO) for Europe ($R = 0.37$, $P < 0.05$); and Pacific Decadal Oscillation (PDO) for
197 Asia ($R = 0.50$, $P < 0.01$) (Supplementary Tables 2 and 3). These three indices are also significantly
198 correlated to global mean annual u ($P < 0.01$; Supplementary Table 2). Furthermore, we conducted
199 Granger causality tests, in which we select lag length using a Bayesian information criterion
200 (Granger, 1969). Global mean annual u is Granger caused by TNA ($P < 0.001$), NAO ($P < 0.01$)
201 and PDO ($P < 0.1$). Regionally, the tests also reject the null hypothesis that TNA does not Granger
202 cause u over North America ($P < 0.001$), NAO does not Granger cause u over Europe ($P < 0.1$),
203 and PDO does not Granger cause u over Asia ($P = 0.11$). Besides, although the reversals of the
204 wind stilling phenomenon in different regions are driven by different climate indices, owing to the
205 ocean/atmosphere oscillations having some degree of synchronization during turning points of
206 multidecadal climate variability (Tsonis et al., 2007; Henriksson, 2018), a global pattern of
207 terrestrial stilling and its reversal emerges (Figs 1 and 2).

208

209 To further uncover the mechanisms behind the decadal variations of u , we construct the composite
210 annual mean surface temperature for the years that exhibit negative (Fig. 3a) and positive (Fig. 3b)
211 anomalies of detrended u . Distinct temperature patterns correspond to both negative and positive
212 u anomalies, but exhibits different spatial patterns across the globe. During the years of negative u
213 anomalies (Fig. 3a) the following are observed: (a) positive anomalies of temperature prevail over
214 Tropical Northern Atlantic (TNA region, 5.5°N to 23.5°N , 15°W to 57.5°W), showing a positive
215 value for TNA; (b) the west (east) Pacific is warmer (colder) than normal years, demonstrating a
216 negative value for PDO; (c) positive anomalies of temperature occur near the Azores and negative

217 anomalies occur over Greenland, indicating a negative value for NAO. The opposite pattern (i.e.
218 negative TNA, positive PDO and NAO) occurs during the years of positive u anomalies (Fig. 3b).
219 The ocean/atmosphere oscillations, characterized as the decadal variations in these climate indices
220 (mainly TNA, NAO, PDO), can therefore explain the decadal variation of u (the long-term stilling
221 and the recent reversal) (Figs 2 and 3f-h).

222

223 The PDO and TNA are important predictors regardless of subset of stations used. Yet, while NAO
224 has the largest explanatory power for regional u over Europe, there are 169/300 cases that NAO is
225 not included as a major predictor (Supplementary Table 3). Thus, even within Europe, the impact
226 of NAO differs regionally. We thus investigate the spatial patterns of the correlation between the
227 three indices (PDO, TNA, NAO) and the regional ($5^\circ \times 5^\circ$) winds (Fig. 3c-e). The regional wind
228 is calculated using all stations within a $5^\circ \times 5^\circ$ cell; and only the cells with more than 3 stations are
229 included in the analysis. TNA has a strong, significant negative correlation with regional u in North
230 America excluding western Canada and areas near Mexico (Fig. 3c). PDO has a significant positive
231 correlation with regional u globally (Fig. 3e). NAO has overwhelmingly significant positive
232 correlation with regional u in the United States and Northern Europe, in particular United
233 Kingdom, but negative correlation with regional u in Southern Europe (Fig. 3d). Statistically, NAO
234 is significantly and negatively correlated with European winds south of 48°N ($R = -0.39$, $P < 0.05$),
235 while significantly and positively correlated with European winds north to 48°N ($R = 0.48$, $P <$
236 0.01).

237

238 There are some theories for the physical mechanisms how the changes in these indices (e.g. TNA,
239 PDO, and NAO) impact on the regional u over land^{22,24,25,27}. With respect to TNA, previous studies

240 demonstrate that the positive phase of TNA is linked with a weakened Hadley circulation²⁴. We
241 also find that during the positive phase of TNA there is a cold anomaly over the eastern coast of
242 the United States (Fig. 3a) (in line with the finding in ref. 24), which leads to a southward
243 component of surface wind and facilitates a stable environment of weak convergence from tropics
244 to the mid-latitude region. Both the effects indicate that a positive TNA will reduce u in the mid-
245 latitudes, the United States in particular (Fig. 3c and Supplementary Fig. 17a,b). As for NAO, the
246 negative and positive phases of NAO have different Jet Stream configurations and wind systems
247 in Northern versus Southern Europe (Supplementary Fig. 17c,d; refer the theory to ref. 22). During
248 the positive phase, a large pressure gradient across the North Atlantic²² generates strong winds and
249 storms across North America (especially the east coast of the United States) and Northern Europe
250 (Supplementary Fig. 17d). Meanwhile, during its negative phase, a small pressure gradient²²
251 produces a weakened jet stream across North America and Southern Europe, yet increases storms
252 in Southern Europe (Supplementary Fig. 17c). This theory explains the contrasting correlations of
253 NAO to u in northern and southern Europe (Fig. 3d, Supplementary Fig. 18). For PDO, the
254 temperature gradient during the negative (positive) phase generates an easterly (westerly)
255 component of surface wind^{25,27}, which weakens (strengthens) the prevailing westerly winds in the
256 mid-latitudes (Supplementary Fig. 17e,f). It explains the widespread and significant positive
257 correlations between PDO and u across the whole mid-latitudes (Fig. 3e).

258

259 Last but not least, it is critical to figure out why global reanalysis products do not reproduce or
260 largely underestimate the historical terrestrial stilling (Supplementary Fig. 1), which is a major
261 basis for the previous studies rejecting the ocean/atmosphere oscillations as a dominant driver for
262 the global terrestrial stilling (e.g. Vartard et al., 2010; Wu et al., 2018). Global reanalysis products

263 have only assimilated sea level pressure data, and thus the capacities of these products in
264 reproducing surface wind speed over land are determined by Global Climate Model (GCM) used
265 in the assimilation systems. Surface process parameterization schemes (e.g. Monin-Obukhov
266 similarity theory) are used to simulate the winds over land in these models, yet these schemes have
267 uncertainties. We find that in the regions where AMIP simulations (i.e. GCM simulations forcing
268 with the observed SST) capture the stilling, such as Europe and India (Fig. 4a,b in Zeng et al.,
269 2018), the global reanalysis products are also capable to reproduce the stilling in these regions (Fig.
270 S1c); while in the regions where AMIP simulations do not capture the stilling, such as North
271 America (Pryor et al., 2009; Zeng et al., 2018), the global reanalysis products fail to reproduce the
272 stilling (Vautard et al., 2010; Torralba et al., 2017) (Fig. S1b). Therefore, it is the model limitations
273 that make global reanalysis products difficult reproducing the observed wind speed changes in
274 some regions. More efforts are required to improve surface process parameterization scheme and
275 its connection to ocean/atmosphere circulations in the climate models.

276

277 **Implications for wind energy of the reversal in global terrestrial stilling**

278 Finally, we explore some implications of these changes for the global wind power industry. In
279 wind power assessments, near-surface wind observations from weather stations (u at the height of
280 $z_r = 10$ meters) are often used to estimate wind speeds at the height of a turbine (u_{tb} at the height
281 of $z_{tb} = 50-150$ meters) using an exponential wind profile power law relationship:

282

$$u_{tb} = u \left(\frac{z_{tb}}{z_r} \right)^\alpha \quad (2)$$

283 where the α is commonly assumed to be constant (1/7) in wind resource assessments because the
284 differences between these two levels are unlikely great enough to introduce considerable errors in
285 the estimates (e.g. refs 5, 28-30).

286
287 Changes in wind speed matter not only on average but also in the percentage of time wind speeds
288 are high or low. A $u > 3 \text{ m s}^{-1}$ is a typical minimum u needed to drive turbines, so wind speeds
289 below 3 m s^{-1} are typically wasted from a power perspective. Although periods of high wind speed
290 greatly increase the physical capacity to generate power according to formula (1), turbines are built
291 with a maximum capacity, so periods of high wind speed can also “waste” the uses of wind with
292 the threshold depending on the capacity of the turbine.

293
294 On average, the increase of global mean annual u from 3.13 m s^{-1} in 2010 to 3.30 m s^{-1} in 2017
295 (Fig. 1a; see *Methods* for details) increases the amount of energy entering a hypothetical wind
296 turbine receiving the global average wind by $17 \pm 2\%$ (uncertainty is associated with subsamples
297 in Fig. 1a; regionally, $22 \pm 2\%$ for North America, $22 \pm 4\%$ for Europe, and $11 \pm 4\%$ for Asia). At
298 the hourly scale, we also find that the frequency of low u ($< 3 \text{ m s}^{-1}$) decreases while the frequency
299 of high u increases (Fig. 4a). Using one General Electric GE 2.5 – 120 turbine³¹ (Supplementary
300 Fig. 19) to illustrate, the effects of changes in global average u increase potential power generation
301 from 2.4 million kWh in 2010 to 2.8 million kWh in 2017 (+17%). If present trend persists for at
302 least another decade, in the light of the robust increasing rate during 2000-2017 (Fig. 1a) and the
303 long cycles of natural ocean/atmosphere oscillations^{22,24,25,27,35} (Supplementary Fig. 20), power
304 would rise to 3.3 million kWh in 2024 (+37%), resulting in a +3% per decade increase of global-
305 average capacity factor (mean power generated divided by rated peak power) on average. This

306 change is even larger than the projected change in wind power potential caused by climate change
307 under multi-scenarios (Tobin et al., 2015, 2016).

308

309 During the past decade, the capacity factor of the U.S. wind fleet³² has steadily risen at a rate of
310 +7% per decade (Fig. 4b), which previous reports have attributed solely to technology
311 innovations³³. We find that the capacity factor for wind generation in the U.S. is highly and
312 significantly correlated with the variation in the cube of regional-average u (u^3 , $R = 0.86$, $P < 0.01$;
313 Fig. 4b). To isolate the u -induced increase in capacity factor from that due to technology
314 innovation, we use the regional mean hourly wind speed in 2010 and 2017 to estimate the increase
315 of capacity factor for a given turbine, thereby controlling for technology innovation. It turns out
316 that the increased u^3 explains ~50% of the increase of the capacity factor (see *Methods* for details).
317 Therefore, in addition to technology innovation, the strengthening u is another key factor powering
318 the increasing reliability of wind power in the U.S. (and other mid-latitude countries where u is
319 increasing, such as China and Europe countries).

320

321 To illustrate the consequences, one turbine (General Electric GE 1.85 – 87 (ref. 34)) installed at
322 one of our *in-situ* weather stations in the U.S. in 2014 (inset plot in Fig. 4c), which was expected
323 to produce 1.8 ± 0.1 million kWh using four years of u records before the installation (2009-2013)³⁴,
324 actually produced 2.2 ± 0.1 million kWh between 2014-2017 (+25%). This system has the potential
325 to generate 2.8 ± 0.1 million kWh (+56%) if u recovers to the 1980s level (red bars in Fig. 4d; see
326 *Methods* for details). Globally, 90% of the global cumulative wind capacity has been installed in
327 the last decade¹³, during which global u has been increasing (see above).

328

329 **Discussion**

330 Although the response of ocean/atmosphere oscillations to greenhouse warming remains unclear²⁷,
331 because these oscillations change over decadal time frames^{22,24,25,27,35}, the increases in wind speeds
332 should continue for at least a decade. Climate model simulations constrained with historical sea
333 surface temperature also show a long cycle in u over land (Supplementary Fig. 20). Our findings
334 are therefore good news for the power industry for the near future.

335

336 However, oscillation patterns in the future will likely cause returns to declining wind speeds, and
337 anticipating these changes should be important for the wind power industry. Wind farms should
338 be constructed in the areas with stable winds and high effective utilization hours (e.g. 3 - 25 m s⁻¹).
339 If high wind speeds are likely to be common, building turbines with larger capacities will often
340 be justified. For example, capturing more available wind energy (blue bars in Fig. 4d) could be
341 achieved through the installation of higher capacity wind turbines (e.g. General Electric GE 2.5 –
342 120, green bars in Fig. 4d), greatly increasing total power generation. Most turbines tend to require
343 replacement after 12-15 years³⁶. Further refinement of the relationships uncovered in this paper
344 could allow choices of turbine capacity, rotor and tower that are optimized not just to wind speeds
345 of the recent past but to likely future changes during the lifespan of the turbines.

346

347 In summary, we find that after several decades of global terrestrial stilling, wind speed has
348 rebounded, increasing rapidly in the recent decade globally since 2010. Ocean/atmosphere
349 oscillations, rather than increased surface roughness, are likely the causes. These findings are
350 important for those vested in maximizing the potential of wind as an alternative energy source.
351 The development of large-scale alternative energy sources such as wind power^{6,9-11,13} is one of the

352 most effective approaches to reduce anthropogenic gas emissions¹⁰ for the goal to keep warming
353 well below 2 °C by the end of the 21st century. One megawatt (MW) of wind power reduces 1,309
354 tonnes of CO₂ emissions and also saves 2,000 liters of water compared with other energy
355 sources^{11,13}. Since its debut in the 1980s, the total global wind power capacity reached 539
356 gigawatts by the end of 2017, and the wind power industry is still booming globally. For instance,
357 the total wind power capacity in the U.S. alone is projected to increase fourfold by 2050 (ref. 11).
358 The reversal in global terrestrial stalling bodes well for the expansion of large-scale and efficient
359 wind power generation systems in these mid-latitude countries in the near future.

360

361 **Methods**

362 **Wind datasets.** The key data used in this analysis is the Global Surface Summary of the Day
363 (GSOD) database processed by the National Climatic Data Center (NCDC) of the United States
364 (download August 1st 2018 from <ftp://ftp.ncdc.noaa.gov/pub/data/g sod>). The database is derived
365 from the United States Air Force (USAF) DATSAV3 Surface data and the Federal Climate
366 Complex Integrated Surface Hourly dataset, which is grounded on data exchanged under the World
367 Meteorological Organization (WMO) World Weather Watch Program according to WMO
368 Resolution 40 (Cg-XII)³⁹. There is a total of 28,149 stations included in the GSOD database
369 globally (for the distributions see the dots in Supplementary Fig. 3). Online data are available from
370 1929 to the present, with data for the past four decades being the most complete. Daily data for
371 each station include mean wind speed, maximum sustained wind speed, maximum wind gust, mean
372 temperature, maximum temperature, minimum temperature, precipitation amount, mean sea-level
373 pressure, mean station pressure, mean dew point, daily mean visibility, snow depth, and the
374 occurrence of the following phenomena: fog, rain or drizzle, snow or ice pellets, hail, thunder, and

375 tornado/funnel clouds. The original records from all the weather stations have undergone extensive
376 quality control procedures (more than 400 algorithms) by the Air Weather Service (see
377 www.ncdc.noaa.gov/isd for details). These synoptic hourly observations were processed into mean
378 daily values from recorded hourly data by the NCDC.

379

380 We focus our study on the decadal variation of u and other wind variables (maximum sustained
381 wind speed, maximum wind gust) for the 40-year period of 1978-2017, when the data are the most
382 complete. In selection of the final subset of stations in this study, we employ strict selection criteria
383 to avoid including incomplete data series. Firstly, we only select stations with complete data for
384 all the 40 years of the analysis (1978-2017), each year with complete records for all the 12 months.
385 Secondly, each monthly value has to be derived from at least 15 days of data. Finally, the daily
386 values have to be derived from a minimum of four observations. As a result, only 1,435 stations
387 are included for analysis (locations of those stations are shown as red dots in Supplementary Fig.
388 3; and the mean number of observations in a day is shown in Supplementary Fig. 10; code and the
389 processed data is available in Supplementary Data 1). Among them, 543 stations are automatic
390 monitoring stations that are in operation during the entire study period. For some analyses
391 (Supplementary Fig. 7) we relax our selection criteria to include more stations – for instance, by
392 allowing 1, 5, 10 or 20 years of missing data. Last, the results show no dependence on whether
393 global mean annual u or global median annual u is used to describe the decadal variation of global
394 u (Supplementary Fig. 21 versus Fig. 1a).

395

396 We also repeat the wind analyses using the HadISD (version v2.0.2.2017f)¹⁹ global sub-daily
397 database, which is distributed by the Met Office Centre and is freely assessed from:

398 <https://www.metoffice.gov.uk/hadobs/hadisd/>. The dataset spans from 1931 to the end of 2017.
399 The total number of stations in HadISD is 8,103, all of which passed quality control tests that are
400 designed to remove bad data while keeping the extremes of wind speed and direction, temperature,
401 dew point temperature, sea-level pressure, and cloud data (total, low, mid and high level). For
402 example, quality control procedures have been performed on the major climatological variables,
403 including a duplicate check, an isolated odd cluster check, a frequent values check, a distributional
404 gap check, a world record check, a streak check, a climatological check, a spike check, a
405 temperature-humidity cross check, a cloud-logical cross check, an excess variance check, and a
406 neighbor outlier check¹⁹. In our analysis, we use the criteria as that described above to select
407 stations that have uninterrupted, continuous monthly records during the period 1978-2017 (n =
408 1,542; code and the processed data is available in Supplementary Data 2).

409
410 **Climate indices.** The dynamics of ocean/atmospheric circulations can be described with climate
411 indices. Almost all climate indices are associated with regional surface temperature anomalies (or
412 temperature heterogeneity) to some extent, in particular sea surface temperature (SST). The
413 anomaly in SST has a profound impact on the climate over land through the tight linkage between
414 the oceans and the atmosphere^{23,40,41}. The oceans, in particular in regions around the equator, act
415 as a massive heat-retaining solar panel providing fundamental energy for the atmospheric engine
416 to transfer the heat from the tropics to the poles through global circulation systems (i.e., Hadley,
417 Ferrel, and polar cells) that have a profound impact on the global climate^{40,42}. Even an apparently
418 small change of SST in just one region can produce major climate variations over large areas of
419 the planet⁴¹. For example, tropical Pacific cooling is found to be the cause of the recent ongoing

420 warming hiatus^{23,43}. In general, regional variations in SST can trigger decadal variations in the
421 climate indices, leading to decadal variations in the Earth's climate system^{23,27,44}.

422

423 We select 21 time series of climate indices describing monthly atmospheric and oceanic
424 phenomena to compare decadal variations of the Earth's climate system with changes in wind
425 speed (Supplementary Table 2). Only indices that are available for the whole study period (1978-
426 2017) are considered (download from <https://www.esrl.noaa.gov/psd/data/climateindices/list/>).
427 For example, we include the following eight teleconnection indices: Pacific Decadal Oscillation
428 (PDO); Pacific North American Index (PNA); Western Pacific Index (WP); North Atlantic
429 Oscillation (NAO); East Pacific/North Pacific Oscillation (EP/NP); North Pacific pattern (NP);
430 East Atlantic pattern (EA); and Scandinavia pattern (SCAND). We include one atmospheric index
431 (Arctic Oscillation (AO)) and one multivariate El Niño–Southern Oscillation (ENSO) index. We
432 include six indices describing regional SST in Pacific oceans: Eastern Tropical Pacific SST (5°N
433 – 5°S, 150° W – 90 °W) (NINO3); Central Tropical Pacific SST (5°N-5°S) (160°E-150°W)
434 (NINO4); Extreme Eastern Tropical Pacific SST (0 – 10°S, 90°W – 80°W) (NINO12); East Central
435 Tropical Pacific SST (5°N – 5°S) (170°W – 120°W) (NINO34); Oceanic Niño Index (ONI); and
436 Western Hemisphere warm pool (WHWP). Two of the indices describe regional SST in Atlantic
437 oceans—the Tropical Northern Atlantic Index (TNA) and the Tropical Southern Atlantic Index
438 (TSA). The final three indices are the Atlantic Meridional Mode (AMM), the Southern Oscillation
439 Index (SOI), and the 10.7-cm Solar Flux (Solar).

440

441 **Statistical analyses.** It is apparent that the trend varies in the time series of global and/or regional
442 average mean annual u for different ranges of year (e.g., Fig. 1a). Traditional single linear model

443 does not provide an adequate description of a change in the tendency. In this study, we apply a
444 piecewise linear regression model^{14,15} to quantify potential turning points in a given time series.
445 Piecewise linear regression is capable of detecting where the slope of a linear function changes,
446 and allows multiple linear models to be fitted to each distinct section of the time series. For a time
447 series y (e.g. global average mean annual u), a continuous piecewise linear regression model with
448 one turning point (TP) can be described as:

$$449 \quad y = \begin{cases} \beta_0 + \beta_1 t + \varepsilon, & t \leq TP \\ \beta_0 + \beta_1 t + \beta_2(t - TP) + \varepsilon, & t > TP \end{cases} \quad (3)$$

450 where t is year; β_0 , β_1 and β_2 are regression coefficients; ε is the residual of the regression.
451 The linear trend is β_1 before the TP (year), and $\beta_1 + \beta_2$ after the TP. We use least square error
452 techniques to fit the model to the data and determine TP, β_0 , β_1 and β_2 . To avoid linear
453 regression in a period with too few years, we confine TP to be within the period of 1980 to 2015.
454 The necessity of introducing TP is tested statistically with the t -test under the null hypothesis that
455 “ β_2 is not different from zero”. The diagnostic statistics for the regression also include the
456 goodness of fit (R^2), the P value for the whole model, and the P values for the trends before and
457 after TP. We consider $P < 0.05$ as significant.

458
459 In addition, we use a forward stepwise regression algorithm²⁶ to select major climate indices that
460 have the largest explanatory power for the decadal variations in u . The algorithm is a systematic
461 method for adding predictors from a multilinear model according to their statistical significance in
462 explaining the response (decadal variation of u in this study). The initial regression model contains
463 only an intercept term. Then, the explanatory power of incrementally larger and smaller models is
464 compared to determine which predictor should be included. At each step, the P-value of an F-

465 statistic is calculated to examine models with a potential predictor that is not already in the model.
466 The null hypothesis is that the predictor would have a zero coefficient if included in the model. If
467 there is sufficient evidence at a given significant level to reject the null hypothesis, the predictor is
468 added to the model. Therefore, the earlier the predictor enters in to the model, the larger the
469 explanatory power the predictor has.

470

471 **Analyses on the possible causes for the decadal variation in wind speed.** Overall, the twenty-
472 one climate indices explain 90% of the multi-decadal scale, year-to-year variation in global mean
473 annual u (adjusted $R^2 = 78\%$). Regionally, they explain 91%, 75% and 87% of the multi-decadal
474 scale, year-to-year variation in mean annual u for North America (adjusted $R^2 = 81\%$), Europe
475 (adjusted $R^2 = 46\%$) and Asia (adjusted $R^2 = 71\%$), respectively. Globally, the indicators
476 significantly correlated with u include TNA ($R = -0.50$; P -value < 0.01), PDO ($R = 0.46$; $P < 0.01$),
477 WHWP ($R = -0.46$; $P < 0.01$), NAO ($R = 0.39$; $P < 0.05$), AMM ($R = -0.39$; $P < 0.05$), EP/NP (R
478 $= 0.37$; $P < 0.05$), TSA ($R = -0.38$; $P < 0.05$), Solar ($R = 0.35$; $P < 0.05$), SOI ($R = -0.32$; $P < 0.05$),
479 and EA ($R = 0.31$; $P < 0.05$). All the significant indicators are determined from the SST anomaly
480 over some regions of the tropics, except NAO and EA which are closely relevant to the Arctic
481 oscillation. Among these indicators, TNA is the most significant indicator for u change over North
482 America ($R = -0.63$; $P < 0.01$); NAO is the most significant indicator for Europe ($R = 0.37$; $P <$
483 0.05); and PDO for Asia ($R = 0.50$; $P < 0.01$) (Supplementary Table 2).

484

485 According to the forward stepwise regression analysis, as for global mean annual u , the first six
486 climate indices include in the model are TNA, PDO, AMM, Solar, WHWP, and SCAND
487 (Supplementary Table 3). Regionally, similar to the correlation analysis, TNA has the largest

488 explanatory power for u over North America; NAO has the largest explanatory power for u over
489 Europe; and PDO has the largest explanatory power for u over Asia (Supplementary Table 3).
490 Furthermore, we randomly select 40% of stations for the calculation of global/regional u and repeat
491 the analyses for 300 times to estimate the uncertainty (number in parentheses in Supplementary
492 Table 3 shows how many times climate indices are selected as six major predictors). Last, the six
493 climate indices explain $70 \pm 5\%$, $79 \pm 3\%$, $48 \pm 9\%$, and $51 \pm 8\%$ of the multi-decadal scale, year-to-
494 year variation in mean annual u for the globe, North America, Europe, and Asia, respectively
495 (Supplementary Table 3, Supplementary Fig. 15).

496

497 **Calculations for wind power assessments.** Due to the nonlinear relationship between wind power
498 (P) and wind speed (u) (Equation (1)), high temporal resolution data are needed for u to produce
499 an accurate estimate of P . Thus, we use the HadISD global sub-daily database from the Met Office
500 Centre¹⁹. For each station that has uninterrupted, continuous monthly records during the period
501 1978-2017 ($n = 1,542$), we use linear interpolation to interpolate a sub-daily time series to an hourly
502 time series. Fig. 4a shows the frequency distributions of global average hourly wind speed in 2010
503 and 2017, and the year 2024, assuming the same increasing rate.

504

505 We then discuss annual wind power production given these wind speed time series (2010, 2017
506 and 2024), considering that production is dependent on the specifications of wind turbines. Here
507 we use General Electric GE 2.5 – 120 (ref. 31) as an example. The parameters for this turbine
508 include the following: rated power, 2,500.0 kW; cut-in wind speed, 3.0 m s^{-1} ; cut-out wind speed,
509 25.0 m s^{-1} ; diameter, 120 m; swept area, $11,309.7 \text{ m}^2$; and hub height: 110/139 m (here we take
510 120 m). The power curve for this turbine is shown in Supplementary Fig. 22. The wind speed time

511 series (2010, 2017 and 2024) at the height of the turbine (i.e. 120 m) are first estimated using the
512 wind profile power law (Equation (2)), and are then converted into the hourly wind power
513 (Supplementary Fig. 19) using the power curve (Supplementary Fig. 22). Owing to the increase
514 frequency of high u , annual wind power production from the turbine increases from 2.4 million
515 kWh in 2010 to 2.8 million kWh in 2017; and to 3.3 million kWh in 2024. As a result, the overall
516 capacity factor increases 1.9% during 2010-2017, and 2.2% during 2018-2024.

517

518 To compare the significance of the increased capacity factor induced by the strengthening u with
519 that due to technology innovation (e.g. improvement of the turbine's power efficiency), we collect
520 the overall capacity factor for wind generation in the U.S. from the U.S. Energy Information
521 Administration³² (the black line in Fig. 4b). In the U.S., the overall capacity factor is highly
522 correlated with the cube of regional wind speed (u^3) ($R = 0.86$, $P < 0.01$; Fig. 4b). Even for the
523 detrended time series, the correlation coefficient between capacity factor and u^3 is as high as 0.71
524 ($P < 0.05$), showing that wind speed is a key factor for the year-to-year variation of wind power
525 energy production. It is well known that technology innovation is a key factor that drives the
526 increase of capacity factor for wind generation³³. To isolate the u -induced increase in capacity
527 factor from that due to technology innovation, we use the regional mean hourly wind speed in
528 2010, 2017 and 2024 (assuming the same increasing rate) to estimate the increase of capacity factor
529 for a given turbine, thereby controlling for technology innovation. The u -induced increase in
530 capacity factor is +2.5% between 2010 and 2017, and +3.2% between 2017 and 2024. It explains
531 more than 50% of the overall increase of capacity factor for wind generation in the United States.

532

533 We also collect information of the installed turbines from the U.S. Wind Turbine Database (n =
534 57,646; <https://eerscmap.usgs.gov/uswtdb>) (locations refer to Supplementary Fig. 23). The turbine
535 with the nearest distance to one of the HadISD weather stations (n = 1,542) is at Deaf Smith
536 County, the U.S. (<1 km; wind farm name: Hereford 1; case ID: 3047384; location see the inset
537 plot in Fig. 4c). The turbine was installed in 2014. The turbine is a General Electric GE 1.85 – 87
538 (ref. 34). The parameters for this turbine include: rated power, 1,850.0 kW; cut-in wind speed, 3.0
539 m s⁻¹; rated wind speed, 12.5 m s⁻¹; cut-out wind speed, 25.0 m s⁻¹; diameter, 87.0 m; swept area,
540 5,945.0 m²; hub height: 80 m. We combine these parameters with Equation (1) to estimate the
541 power curve for the turbine (Supplementary Fig. 24). Finally, we integrate the power curve with
542 the hourly wind speed from 1978 to 2017 at the hub height at this station to calculate annual wind
543 power production generated by the General Electric GE 1.85 – 87 turbine (Supplementary Fig.
544 25a; red bars in Fig. 4d). In addition, we calculate annual wind power production at the station
545 generated by the General Electric GE 2.5 – 120 turbine (Supplementary Fig. 25b; green bars in
546 Fig. 4d). We also use the Equation (1) to estimate maximum annual wind power production at the
547 station given diameter of 120 m and hub height of 120 m (the same as the General Electric GE 2.5
548 – 120 turbine), which is constrained by the Betz Limit ($f = 16/27$ in Equation (1)) (Supplementary
549 Fig. 25c; blue bars in Fig. 4d). The Betz Limit describes the theoretical maximum ratio of power
550 that can be extracted by a wind turbine to the total power contained in the wind.

551

552 **Data availability.** The data for quantifying wind speed changes are the Global Surface Summary
553 of the Day database (GSOD, <ftp://ftp.ncdc.noaa.gov/pub/data/g sod>), and the HadISD (version
554 v2.0.2.2017f) global sub-daily database (<https://www.metoffice.gov.uk/hadobs/hadisd/>). The time
555 series of climate indices describing monthly atmospheric and oceanic phenomena are obtained

556 from the National Oceanic and Atmospheric Administration
557 (<https://www.esrl.noaa.gov/psd/data/climateindices/list/>). Simulated wind speed changes in
558 Coupled Model Intercomparison Project Phase 5 (CMIP5) are available in the Program for Climate
559 Model Diagnosis and Intercomparison (<https://esgf-node.llnl.gov/projects/cmip5/>). Simulated
560 wind speed changes constrained by historical sea surface temperature are provided by the IPSL
561 Dynamic Meteorology Laboratory. Wind records in reanalysis products include the ECMWF
562 ERA-Interim Product (<apps.ecmwf.int/datasets/data/interim-full-daily/>) and the NCEP/NCAR
563 Global Reanalysis Product (<http://rda.ucar.edu/datasets/ds090.0/>). The processed wind records and
564 the relevant code are available in Supplementary Data 1 and 2. All datasets are also available on
565 request from Z. Zeng.

566

567 **Code availability.** The program used to generate all the results is MATLAB (R2014a) and ArcGIS
568 (10.4). Analysis scripts are available by request from Z. Zeng. The code producing wind records
569 are available in Supplementary Data 1 and 2.

570
571
572
573
574
575
576
577
578
579
580
581
582
583
584
585
586
587
588
589
590
591
592

References.

1. Roderick, M. L., Rotstayn, L. D., Farquhar, G. D. & Hobbins, M. T. On the attribution of changing pan evaporation. *Geophys. Res. Lett.* **34**, 1–6 (2007).
2. Vautard, R., Cattiaux, J., Yiou, P., Thépaut, J. N. & Ciais, P. Northern Hemisphere atmospheric stilling partly attributed to an increase in surface roughness. *Nat. Geosci.* **3**, 756–761 (2010).
3. Mcvicar, T. R., Roderick, M. L., Donohue, R. J. & Van Niel, T. G. Less bluster ahead? ecohydrological implications of global trends of terrestrial near-surface wind speeds. *Ecohydrology* **5**, 381–388 (2012).
4. McVicar, T. R. *et al.* Global review and synthesis of trends in observed terrestrial near-surface wind speeds: Implications for evaporation. *J. Hydrol.* **416–417**, 182–205 (2012).
5. Tian, Q., Huang, G., Hu, K., & Niyogi, D. Observed and global climate model based changes in wind power potential over the Northern Hemisphere during 1979–2016. *Energy* doi: <https://doi.org/10.1016/j.energy.2018.11.027> (2018).
6. Lu, X., McElroy, M. B. & Kiviluoma, J. Global potential for wind-generated electricity. *Proc. Natl. Acad. Sci.* **106**, 10933–10938 (2009).
7. Zhu, Z. *et al.* Greening of the Earth and its drivers. *Nat. Clim. Chang.* **6**, 791–796 (2016).
8. Torralba, V., Doblas-Reyes, F. J. & Gonzalez-Reviriego, N. Uncertainty in recent near-surface wind speed trends: a global reanalysis intercomparison. *Environ. Res. Lett.* **12**, 114019 (2017).
9. UNFCCC. *Adoption of the Paris Agreement* (FCCC/CP/2015/L.9/Rev.1., 2015).
10. IPCC. *Summary for policymakers in Climate change 2014: Mitigation of climate change. Contribution of working group III to the fifth assessment report of the Intergovernmental Panel on Climate Change* (O. Edenhofer et al., Eds., Cambridge University Press, Cambridge, UK and New York, USA, 2014).

- 593 11. U.S. Department of Energy. *Projected growth wind industry now until 2050* (Washington,
594 D.C., 2018).
- 595 12. Nathan, R. & Muller-landau, H. C. Spatial patterns of seed dispersal, their determinants and
596 consequences for recruitment. *Trends Ecol. Evol.* **15**, 278–285 (2000).
- 597 13. Global Wind Energy Council. *Global Wind Energy Outlook 2018* (2018).
- 598 14. Toms, J. D. & Lesperance, M. L. Piecewise regression: a tool for identifying ecological
599 thresholds. *Ecology* **84**, 2034–2041 (2003).
- 600 15. Ryan, S. E. & Porth, L. S. *A tutorial on the piecewise regression approach applied to bedload*
601 *transport data* (2007).
- 602 16. Azorin-Molina, C. *et al.* Homogenization and assessment of observed near-surface wind speed
603 trends over Spain and Portugal, 1961–2011. *J. Clim.* **27**, 3692–3712 (2014).
- 604 17. Kim, J. C. & Paik, K. Recent recovery of surface wind speed after decadal decrease: a focus
605 on South Korea. *Clim. Dyn.* **45**, 1699–1712 (2015).
- 606 18. Azorin-Molina, C., Dunn, R. J. H., Mears, C. A., Berrisford, P. & McVicar, T. R. 2018: [Global
607 climate; Atmospheric circulation] Surface winds [in “State of the Climate in 2017”]. *Bull. Am.*
608 *Meteorol. Soc.* **99**, S41–S43, doi: 10.1175/2018BAMSStateoftheClimate (2018).
- 609 19. Dunn, R. J. H., Willett, K. M., Morice, C. P. & Parker, D. E. Pairwise homogeneity assessment
610 of HadISD. *Clim. Past* **10**, 1501–1522 (2014).
- 611 20. Zeng, Z. *et al.* Global terrestrial stilling: does Earth’s greening play a role? *Environ. Res. Lett.*
612 Accepted (2018).
- 613 21. Held, I. M., Ting, M. & Wang, H. Northern winter stationary waves: Theory and modeling. *J.*
614 *Clim.* **15**, 2125–2144 (2002).
- 615 22. Hurrell, J. W., Kushnir, Y., Ottensen, G. & Visbeck, M. *The North Atlantic Oscillation climatic*

616 *significance and environmental impact* (eds. Hurrell, J. W., Kushnir, Y., Ottersen, G. & Visbeck,
617 M., 2003).

618 23. Kosaka, Y. & Xie, S. P. Recent global-warming hiatus tied to equatorial Pacific surface
619 cooling. *Nature* **501**, 403–407 (2013).

620 24. Wang, C. Z. Atlantic climate variability and its associated atmospheric circulation cells. *J.*
621 *Clim.* **15**, 1516–1536 (2002).

622 25. Zhang, Y., Xie, S.-P., Kosaka, Y. & Yang, J.-C. Pacific Decadal Oscillation: Tropical Pacific
623 Forcing versus Internal Variability. *J. Clim.* **31**, 8265–8279 (2018).

624 26. Draper, N. R. & Smith, H. *Applied Regression Analysis, 3rd Edition* (Wiley-Interscience,
625 1998).

626 27. Timmermann, A. *et al.* El Niño-Southern Oscillation complexity. *Nature* **559**, 535–545 (2018).

627 28. Archer, C. L. Evaluation of global wind power. *J. Geophys. Res.* **110**, D12110 (2005).

628 29. Elliott, D. L., Holladay, C. G., Barchet, W. R., Foote, H. P. & Sandusky, W. F. *Wind Energy*
629 *Resource Atlas of the United States* (1986).

630 30. Peterson, E. W. & Hennessey, J. P. On the use of power laws for estimates of wind power
631 potential. *Journal of Applied Meteorology* **17**, 390–394 (1978).

632 31. Wind-turbine-models.com. General Electric GE 2.5 - 120. (2018). at <[https://www.en.wind-](https://www.en.wind-turbine-models.com/turbines/310-general-electric-ge-2.5-120)
633 [turbine-models.com/turbines/310-general-electric-ge-2.5-120](https://www.en.wind-turbine-models.com/turbines/310-general-electric-ge-2.5-120)>

634 32. U.S. Energy Information Administration. Capacity Factors for Utility Scale Generators Not
635 Primarily Using Fossil Fuels, January 2013-August 2018. (2018). at
636 <https://www.eia.gov/electricity/monthly/epm_table_grapher.php?t=epmt_6_07_b>

637 33. Dell, J. & Klippenstein, M. Wind Power Could Blow Past Hydro’s Capacity Factor by 2020.
638 (2018). at <<https://www.greentechmedia.com/articles/read/wind-power-could-blow-past-hydros->

- 639 capacity-factor-by-2020>
- 640 34. Wind-turbine-models.com. General Electric GE 1.85 - 87. (2018). at [https://www.en.wind-](https://www.en.wind-turbine-models.com/turbines/745-general-electric-ge-1.85-87)
- 641 [turbine-models.com/turbines/745-general-electric-ge-1.85-87](https://www.en.wind-turbine-models.com/turbines/745-general-electric-ge-1.85-87)
- 642 35. Steinman, B. A. *et al.* Atlantic and Pacific multidecadal oscillations and Northern Hemisphere
- 643 temperatures. *Science* **347**, 988-991(2015).
- 644 36. Hughes, G. *The Performance of Wind Farms in the United Kingdom and Denmark* (the
- 645 Renewable Energy Foundation, 2012).
- 646 37. Morice, C. P., Kennedy, J. J., Rayner, N. A. & Jones, P. D. Quantifying uncertainties in global
- 647 and regional temperature change using an ensemble of observational estimates: The HadCRUT4
- 648 data set. *J. Geophys. Res. Atmos.* **117**, 1–22 (2012).
- 649 38. Reynolds, R. W., Rayner, N. A., Smith, T. M., Stokes, D. C. & Wang, W. An improved in situ
- 650 and satellite SST analysis for climate. *J. Clim.* **15**, 1609–1625 (2002).
- 651 39. WMO Resolution 40 (Cg-XII). *Exchanging meteorological data: Guidelines on relationships*
- 652 *in commercial meteorological Activities: WMO policy and practice* (WMO, 1996).
- 653 40. Wallace, J. & Hobbs, P. *Atmospheric science: an introductory survey* (Academic Press, 2006).
- 654 41. News, O. S. & Atlantic, N. Surface warming hiatus caused by increased heat uptake across
- 655 multiple ocean basins. *Geophys. Res. Lett.* **41**, 7868–7874 (2014).
- 656 42. Makarieva, A. M., Gorshkov, V. G., Sheil, D., Nobre, A. D. & Li, B. L. Where do winds come
- 657 from? A new theory on how water vapor condensation influences atmospheric pressure and
- 658 dynamics. *Atmos. Chem. Phys.* **13**, 1039–1056 (2013).
- 659 43. England, M. H. *et al.* Recent intensification of wind-driven circulation in the Pacific and the
- 660 ongoing warming hiatus. *Nat. Clim. Chang.* **4**, 222–227 (2014).
- 661 44. Chang, P., Ji, L. & Li, H. A decadal climate variation in the tropical Atlantic Ocean from

662 thermodynamic air-sea interactions. *Nature* **385**, 516 (1997).

663 45. European Centre for Medium-Range Weather Forecasts, ERA-Interim Project,
664 <https://doi.org/10.5065/D6CR5RD9>, Research Data Archive at the National Center for
665 Atmospheric Research, Computational and Information Systems Laboratory, Boulder, Colo.
666 (Updated monthly.) Accessed 10 AUG 2018.

667 46. National Centers for Environmental Prediction/National Weather Service/NOAA/U.S.
668 Department of Commerce, NCEP/NCAR Global Reanalysis Products, 1948-continuing,
669 <http://rda.ucar.edu/datasets/ds090.0/>, Research Data Archive at the National Center for
670 Atmospheric Research, Computational and Information Systems Laboratory, Boulder, Colo.
671 (Updated monthly.) Accessed 10 AUG 2018.

672 47. Zhu, Z. *et al.* Global data sets of vegetation leaf area index (LAI)_{3g} and fraction of
673 photosynthetically active radiation (FPAR)_{3g} derived from global inventory modeling and
674 mapping studies (GIMMS) normalized difference vegetation index (NDVI_{3G}) for the period 1981
675 to 2011. *Remote Sens.* **5**, 927–948 (2013).

676 48. Liu, X. *et al.* High-resolution multi-temporal mapping of global urban land using Landsat
677 images based on the Google Earth Engine Platform. *Remote Sens. Environ.* **209**, 227–239 (2018).

678 Pettitt AN. 1979. A non-parametric approach to the change-point problem. *J. R. Stat. Soc. Ser. C:*
679 *Appl. Stat.* 28(2): 126–135. <https://doi.org/10.2307/2346729>.

680 Copernicus Climate Change Service (C3S) (2017): ERA5: Fifth generation of ECMWF
681 atmospheric reanalyses of the global climate . Copernicus Climate Change Service Climate Data
682 Store (CDS), date of access. <https://cds.climate.copernicus.eu/cdsapp#!/home>

683 Tsonis, A. A., et al. (2007). "A new dynamical mechanism for major climate shifts." *Geophysical*
684 *Research Letters* 34(13): n/a-n/a.

685 Henriksson, S. V. (2018). "Interannual oscillations and sudden shifts in observed and modeled
686 climate." *Atmospheric Science Letters* 19(10): e850.

687 Wu, J., Zha, J. L., Zhao, D. M., & Yang, Q. D. Changes in terrestrial near-surface wind speed and
688 their possible causes: an overview. *Climate Dynamics* 51, 2039-2078 (2018).

689 Granger, C.W.J., 1969. "Investigating causal relations by econometric models and cross-spectral
690 methods". *Econometrica* 37 (3), 424–438.

691 Pryor SC, Barthelmie RJ, Young DT, Takle ES, Arritt RW, Flory D, Gutowski WJ Jr, Nunes A,
692 Roads J. 2009. Wind speed trends over the contiguous USA. *Journal of Geophysical Research -*
693 *Atmospheres* 114: D14105, DOI: 10.1029/2008JD011416

694

695

696
697
698
699
700
701
702
703
704
705
706
707
708
709
710
711
712
713
714
715
716
717

Additional information

Supplementary information is available in the online version of the paper. Reprints and permissions information is available online at www.nature.com/reprints.

Correspondence and requests for materials should be addressed to Z. Zeng.

Acknowledgements

This study was supported by Lamsam-Thailand Sustain Development (B0891). J. Liu was supported by the National Natural Science Foundation of China (41625001). We thank Della Research Computing in Princeton University for providing computing resources. We thank the USA? National Climatic Data Center and the UK Met Office Centre for providing surface wind speed measurements, and thank the Program for Climate Model Diagnosis and Intercomparison and the IPSL Dynamic Meteorology Laboratory for providing surface wind speed simulations.

Author contributions

Z. Zeng and E. Wood designed the research. Z. Zeng and L. Yang performed analysis; Z. Zeng, A. Ziegler, T. Searchinger wrote the draft; and all the authors contributed to the interpretation of the results and the writing of the paper.

Competing financial interests

The authors declare no competing financial interests.

718

Figure Legends.

719

Figure 1. Turning point for mean global surface wind speed (u). (a) Global mean annual u during 1978-2017 (black dot and line). The piecewise linear regression model indicates a statistically significant turning point in 2010. The red line is the piecewise linear fit ($R^2 = 90\%$, $P < 0.001$). The dashed line indicates the turning point. The trends before and after the turning point are shown in the inset. Each grey line ($n = 300$) is a piecewise linear fit for a randomly selected subset (40%) of the global stations. (b) Frequency distribution of the estimated turning points derived from the 300 resampling results. (c) Frequency distribution of the trends in mean annual u before and after the turning point from the 300 resampling results. The result is grounded on the weather stations in the GSOD database.

728

Figure 2. Factors driving the decadal variations in u . Observed (red) and reconstructed (black) detrended mean annual u over the following: (a) the globe, (b) North America, (c) Europe, and (d) Asia. For the globe and each of the three continents, we select six largest explanatory climate indices for the decadal variations of u with a stepwise forwarding regression model. The selected climate indices are then used to reconstruct decadal variations of u via a multiple regression. Uncertainties are the inter-quartile range of the results based on a randomly selected 40% subset of the station pools (repeated 300 times). Inset plots indicate the locations of the stations. The models are trained only using the detrended time series before the turning points. The dashed line indicates the turning point (2010 for the globe, 2012 for North America, 2003 for Europe, and 2001 for Asia). Inset black numbers are coefficients of determination between observed and

737

738 reconstructed u before the turning points. Inset red numbers are correlation coefficient and its
739 significance between observed and reconstructed u after the turning points.

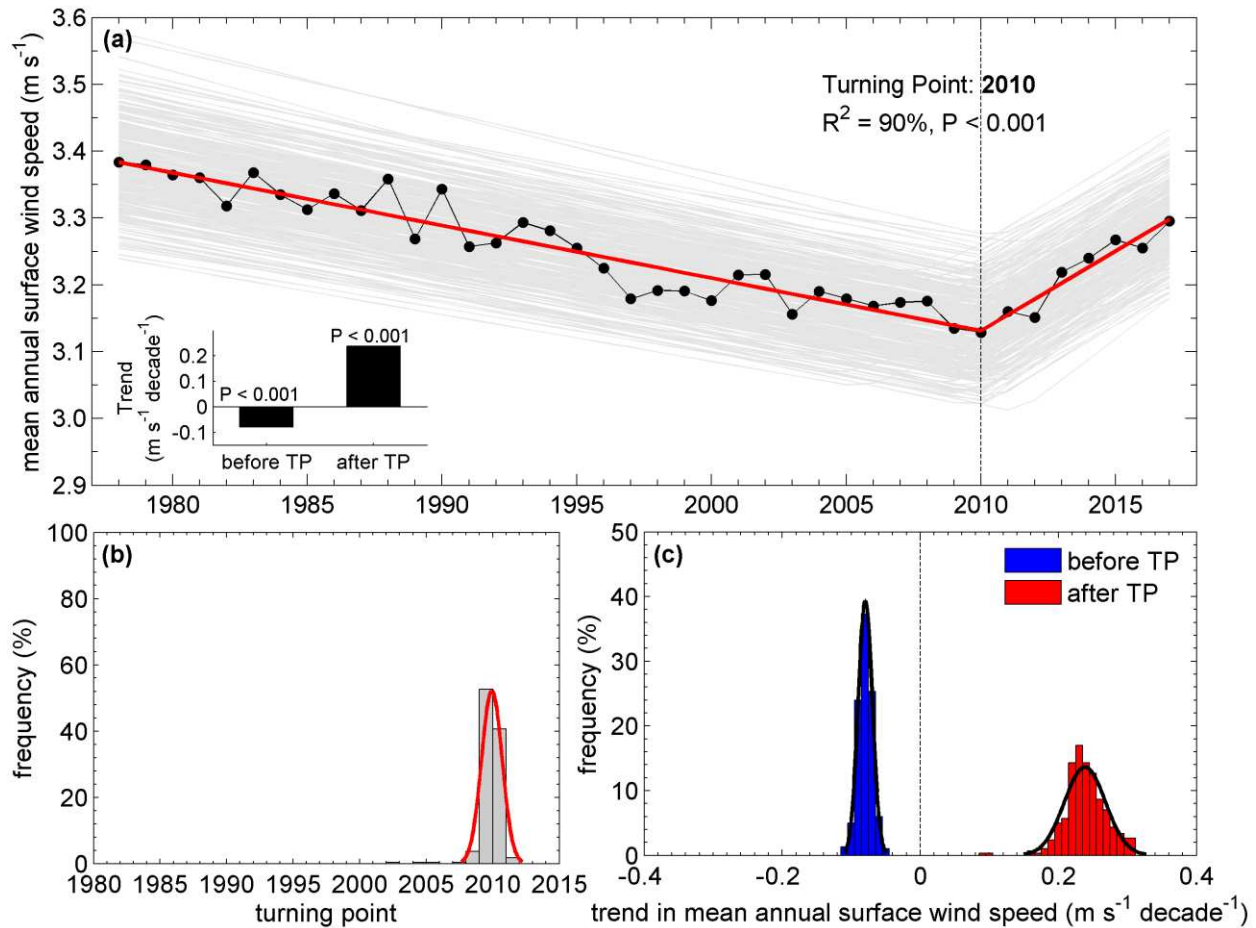
740 **Figure 3. Mechanisms for the decadal variation in u .** Normalized mean annual surface
741 temperature for the years with negative (**a**) and positive (**b**) anomalies of detrended wind.
742 Characteristic regions for Pacific Decadal Oscillation (PDO), North Atlantic Oscillation (NAO)
743 and Tropical Northern Atlantic Index (TNA) are outlined by green, red, and blue boxes,
744 respectively. Surface temperature over land is obtained from Climate Research Unit TEM4 with a
745 spatial resolution of 5° by 5° (ref. 37), and that over ocean is from NOAA Optimum Interpolation
746 (OI) Sea Surface Temperature V2, with a spatial resolution of 1° by 1° (ref. 38). Spatial patterns
747 of the correlation between the regional ($5^\circ \times 5^\circ$) mean annual u and the following: (**c**) TNA; (**d**)
748 NAO; and (**e**) PDO for 1978-2017. Dotting represents significant at $P < 0.05$ level. Decadal
749 variations are shown in panels (**f**) for TNA and regional u in North America; (**g**) for NAO and
750 regional u in Europe; and (**h**) for PDO and regional u in Asia. The thin lines are annual values; and
751 the thick lines are 9-year-window moving averages. The black lines are wind speed; and each of
752 the colored lines are TNA, NAO, and PDO, respectively.

753 **Figure 4. Implications of the recent reversal in global terrestrial stilling for wind energy**
754 **industry.** (**a**) Frequency distribution of global average hourly u in 2010 and 2017, and the year
755 2024 assuming the same increasing rate. (**b**) Time series of the overall capacity factor for wind
756 generation in the U.S. (black line) and the three-order of the regional-average u (u^3 ; blue line) from
757 2008 to 2017. The inset scatter plot shows the significant relationship between the overall capacity
758 factor and the regional u^3 ($R = 0.86$, $P < 0.01$). The inset black numbers show the trend in the
759 overall capacity factor for wind generation, and the inset red numbers show the u -induced increase
760 of capacity factor in the USA. (**c**) Mean annual u observed at a weather station near an installed

761 turbine at Deaf Smith County, USA. (<1 km). The inset plot shows the location. The turbine was
762 installed in 2014. The background colors separate different periods: P0, the 1980s level when u is
763 relative strong (1978-1995); P1, the evaluation years before the installation of the turbine (2009-
764 2013); P2, the operation years when the turbine is generating power (2014-2017). **(d)** Mean annual
765 wind power production at Deaf Smith County, the U.S. from different wind turbines during
766 different periods (red: General Electric GE 1.85 – 87; green: General Electric GE 2.5 – 120 turbine;
767 blue: the theoretical maximum ratio of power that can be extracted by a wind turbine given
768 diameter of 120 m and hub height of 120 m). Error bars show the interannual variability within the
769 periods.

770

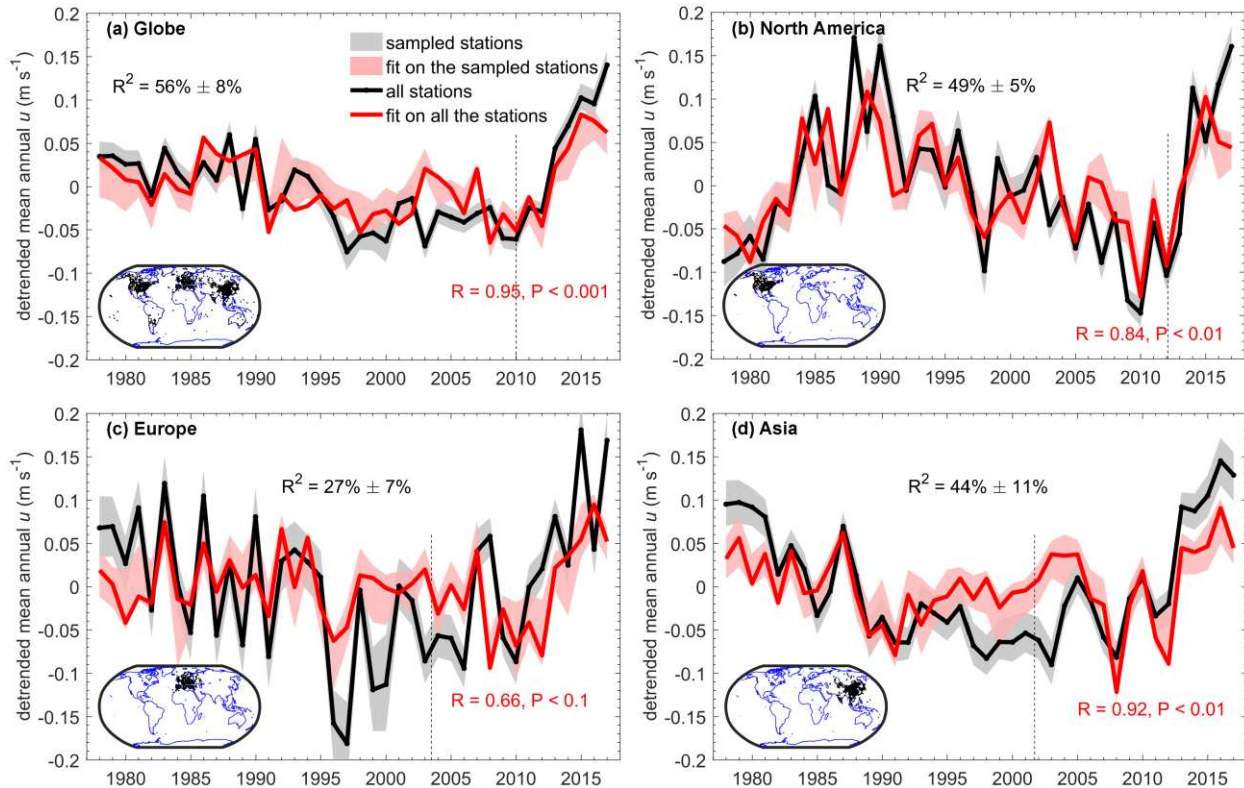
771



772 **Figure 1. Turning point for mean global surface wind speed (u).** (a) Global mean annual u
 773 during 1978-2017 (black dot and line). The piecewise linear regression model indicates a
 774 statistically significant turning point in 2010. The red line is the piecewise linear fit ($R^2 = 90\%$, P
 775 < 0.001). The dashed line indicates the turning point. The trends before and after the turning point
 776 are shown in the inset. Each grey line ($n = 300$) is a piecewise linear fit for a randomly selected
 777 subset (40%) of the global stations. (b) Frequency distribution of the estimated turning points
 778 derived from the 300 resampling results. (c) Frequency distribution of the trends in mean annual
 779 u before and after the turning point from the 300 resampling results. The result is based on the
 780 weather stations in the GSOD database.

781

782

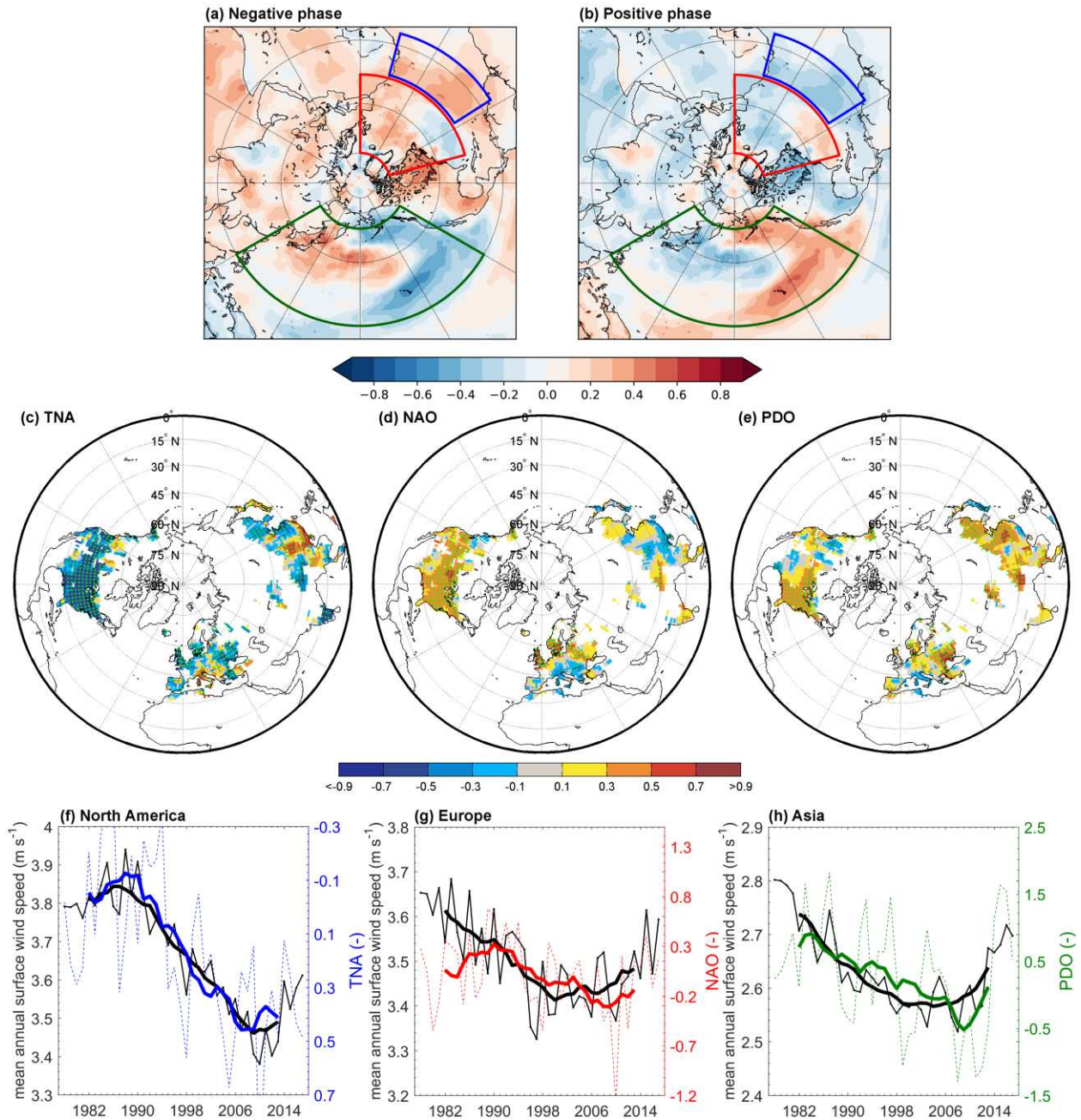


783 **Figure 2. Factors driving the decadal variations in u .** Observed (red) and reconstructed (black)
 784 detrended mean annual u over the following: (a) the globe, (b) North America, (c) Europe, and (d)
 785 Asia. For the globe and each of the three continents, we select six largest explanatory climate
 786 indices for the decadal variations of u with a stepwise forwarding regression model. The selected
 787 climate indices are then used to reconstruct decadal variations of u via a multiple regression.
 788 Uncertainties are the inter-quartile range of the results based on a randomly selected 40% subset
 789 of the station pools (repeated 300 times). Inset plots indicate the locations of the stations. The
 790 models are trained only using the detrended time series before the turning points. The dashed line
 791 indicates the turning point (2010 for the globe, 2012 for North America, 2003 for Europe, and
 792 2001 for Asia). Inset black numbers are coefficients of determination between observed and

793 reconstructed u before the turning points. Inset red numbers are correlation coefficient and its
794 significance between observed and reconstructed u after the turning points.

795

796

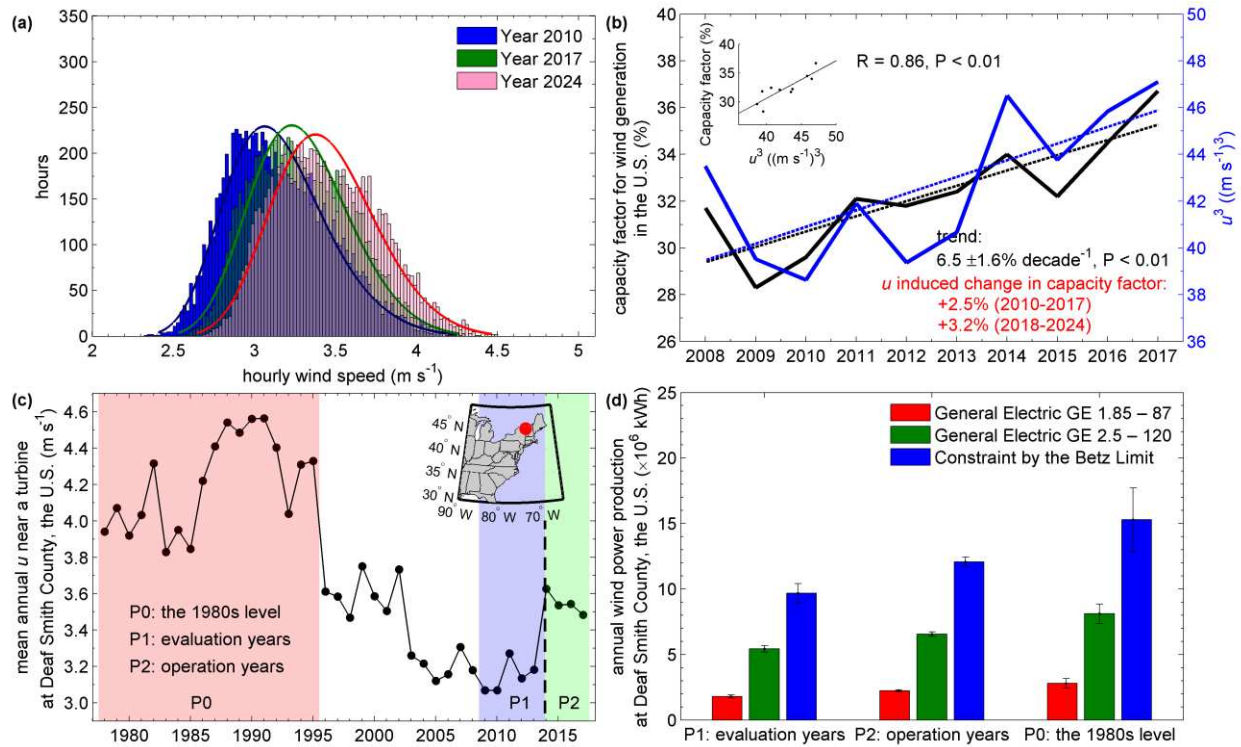


797 **Figure 3. Mechanisms for the decadal variation in u .** Normalized mean annual surface
 798 temperature for the years with negative (a) and positive (b) anomalies of detrended wind.
 799 Characteristic regions for Pacific Decadal Oscillation (PDO), North Atlantic Oscillation (NAO)
 800 and Tropical Northern Atlantic Index (TNA) are outlined by green, red, and blue boxes,
 801 respectively. Surface temperature over land is obtained from Climate Research Unit TEM4 with a

802 spatial resolution of 5° by 5° (ref. 37), and that over ocean is from NOAA Optimum Interpolation
803 (OI) Sea Surface Temperature V2, with a spatial resolution of 1° by 1° (ref. 38). Spatial patterns
804 of the correlation between the regional ($5^\circ \times 5^\circ$) mean annual u and the following: (c) TNA; (d)
805 NAO; and (e) PDO for 1978-2017. Dotting represents significant at $P < 0.05$ level. Decadal
806 variations are shown in panels (f) for TNA and regional u in North America; (g) for NAO and
807 regional u in Europe; and (h) for PDO and regional u in Asia. The thin lines are annual values; and
808 the thick lines are 9-year-window moving averages. The black lines are wind speed; and each of
809 the colored lines are TNA, NAO, and PDO, respectively.

810

811



812 **Figure 4. Implications of the recent reversal in global terrestrial stilling for wind energy**
 813 **industry.** (a) Frequency distribution of global average hourly u in 2010 and 2017, and the year
 814 2024 assuming the same increasing rate. (b) Time series of the overall capacity factor for wind
 815 generation in the U.S. (black line) and the three-order of the regional-average u (u^3 ; blue line) from
 816 2008 to 2017. The inset scatter plot shows the significant relationship between the overall capacity
 817 factor and the regional u^3 ($R = 0.86, P < 0.01$). The inset black numbers show the trend in the
 818 overall capacity factor for wind generation, and the inset red numbers show the u -induced increase
 819 of capacity factor in the United States. (c) Mean annual u observed at a weather station near an
 820 installed turbine at Deaf Smith County, the U.S. (<1 km). The inset plot shows the location. The
 821 turbine was installed in 2014. The background colors separate different periods: P0, the 1980s
 822 level when u is relative strong (1978-1995); P1, the evaluation years before the installation of the
 823 turbine (2009-2013); P2, the operation years when the turbine is generating power (2014-2017).
 824 (d) Mean annual wind power production at Deaf Smith County, the U.S. from different wind

825 turbines during different periods (red: General Electric GE 1.85 – 87; green: General Electric GE
826 2.5 – 120 turbine; blue: the theoretical maximum ratio of power that can be extracted by a wind
827 turbine given diameter of 120 m and hub height of 120 m). Error bars show the interannual
828 variability within the periods.

829